

# A monolithic localized high-order ALE finite element method for multi-scale fluid-structure interaction problems

Lingyue Shen <sup>\*1</sup>, Qi Xin <sup>\*2,3</sup>, Yan Chen<sup>1</sup>, Jiarui Han <sup>†1</sup>, Yumiao Zhang<sup>1</sup>, Jinchao Xu<sup>4</sup>, and Shihua Gong <sup>†2,3</sup>

<sup>1</sup>*Shenzhen Raymind Biotechnology Co., Ltd., Shenzhen, Guangdong 518129, China*

<sup>2</sup>*School of Science and Engineering, The Chinese University of Hong Kong, Shenzhen, Guangdong 518172, China*

<sup>3</sup>*Shenzhen International Center for Industrial and Applied Mathematics, Shenzhen Research Institute of Big Data, Guangdong 518172, China*

<sup>4</sup>*Applied Mathematics and Computational Sciences, CEMSE Division, King Abdullah University of Science and Technology, Thuwal 23955, Saudi Arabia*

## Abstract

This paper presents MLH-ALE, a monolithic localized high-order arbitrary Lagrangian-Eulerian finite element method for multi-scale fluid-structure interaction (FSI). The framework employs isoparametric  $\mathcal{P}_2$  elements for geometric fidelity and an implicit-explicit partitioned Runge-Kutta (IMEX-PRK) scheme for temporal discretization. To address scale disparity, a localized updating strategy is integrated to focus computational resolution on the moving structure. Numerical benchmarks confirm the optimal high-order convergence of the underlying ALE scheme. Furthermore, simulations of particle focusing in spiral microchannels demonstrate that the MLH-ALE approach provides reliable numerical results in good agreement with experimental observations, confirming its feasibility for complex multi-scale applications.

## 1 Introduction

Fluid-structure interaction (FSI) computations play a critical role in guiding industrial advancements in aerospace [14, 17], naval architecture [31] and biomedical research [1, 25, 39, 36], etc. Aerodynamic modeling of aircraft wings is the most common application of FSI simulations in the aerospace [14, 17]. Recently, studies have been published focusing on the use of FSI simulation to assist drone design [10, 15]. In the shipbuilding industry, FSI simulations are employed to model the collision between solids, such as ice blocks, and the ship hull, with the aim of optimizing the hull structure [34, 20, 31]. In biomedical research, FSI simulation has been used in modeling the cell behavior in blood flow [1, 25].

In recent years, research on biological microfluidic devices has grown rapidly [28, 7, 5, 27]. The operating principle of these devices is to precisely control the trajectories or dynamical states of small particles in

---

<sup>\*</sup>These authors contributed equally to this work.

<sup>†</sup>Corresponding author: han@raymind.com, gongshihua@cuhk.edu.cn

flow by manipulating the microscale flow field within the microfluidic chip. This technology has important applications in areas such as medical diagnostics, including the separation of cancer cells [33, 13, 3], the encapsulation of individual cells [9, 41], etc. Owing to the high requirements of flow control and particle motion accuracy in these systems, FSI simulation holds great potential for improving both design efficiency and performance optimization. However, FSI simulations are now facing challenges in two aspects. The first challenge lies in the multiscale nature of the simulation. In microfluidic devices, the characteristic size of the chip typically differs from that of the suspended particles by several orders of magnitude. In addition, the device geometry is often asymmetric [33], which prevents the use of periodic boundary conditions in the simulations. The second challenge is accurately capturing the large translational motion of particles. In microfluidic simulations, particles often undergo long-range migration. This requires an algorithm capable of precisely updating particle positions throughout the simulation. The final challenge is to accurately represent the geometry of the fluid–structure interface since the simulation results of some devices with microscale substructures, such as deterministic lateral displacement (DLD) [23, 16] structures, can be strongly affected by particle geometry. This makes precise geometric characterization essential. So far, there has been very limited algorithmic research towards this situation. In this work, we propose an FSI algorithm specifically designed to handle this situation.

Computing methods developed for general FSI problem are various. Immersed boundary method (IBM) is one of the most popular methods based on Cartesian grid [29, 35]. During the simulation, the grid of the calculation domain keeps unchanged, making the computation very efficient. Also, the data structure based on a structured grid provides excellent scalability, making it well-suited for large-scale parallel computing and GPU acceleration. However, the unchanged grid also presents a limitation when dealing with structures with complex geometries [30].

Recently, diffuse interface methods such as phase-field and level set method have been increasingly reported in solving FSI problem [22, 12, 32, 24]. Compared with IBM, these methods offers significant advantages in managing complex topological transformations. The fluid and structure are identified by different values of phase order. By employing a continuous order parameter, these methods ensures thermodynamic consistency and avoids the numerical oscillations often associated with the discrete force-coupling in IBM. Furthermore, the order parameter characterizes the fluid-structure system as a unified continuum, enabling it to be solved in a monolithic manner.

In contrast to the aforementioned fixed-grid approaches, the Arbitrary Lagrangian-Eulerian (ALE) method [11] and the Deforming-Spatial-Domain/Stabilized Space-Time (DSD/SST) method [38] utilize a dynamic mesh framework that evolves in tandem with structural motion. While IBM and diffuse interface methods simplify grid generation by treating the boundary as a force term or a phase transition on a stationary mesh, they often suffer from smearing effects at the interface [26]. Conversely, the ALE and DSD/SST techniques explicitly track the solid-fluid interface by maintaining a body-fitted mesh that ensures the computational nodes align precisely with the physical boundaries [38, 6, 21], which highly increase the resolution of and accuracy of the physical phenomenon at the fluid-structure interface during the dynamic simulation process. This advantage facilitates the calculation of interfacial stresses and wall shear forces. However, it should be noted that such high-fidelity tracking strongly relies on robust mesh update strategies or local remeshing to prevent element inversion during extreme structural deformations.

Based on the aforementioned research and methodology, this study introduces a monolithic sharp interface

model based on ALE framework. The proposed framework solves a coupled system of fluid and solid in a monolithic manner. The deformation and displacement of the solid are represented by the transport equation for the Cauchy-Green tensor coupled in the system and implemented through a dynamic mesh. To accommodate multi-scale FSI simulations, we have also introduced a new local updating algorithm that is suitable for long-range free structure motion in low Reynolds number flow.

To further enhance temporal stability and accuracy, we reformulate the ALE-based weak form by mapping the governing equations from the time-dependent domain back to a fixed reference configuration (either the initial state or the last remeshed configuration). This transformation effectively converts the evolving-domain problem into one defined on a stationary domain, providing a more rigorous framework for high-order temporal integration. Within this context, a Partitioned Runge-Kutta (PRK) scheme based on an Implicit-Explicit (IMEX) strategy [18] is implemented. This approach achieves high-order temporal precision while efficiently handling the disparate scales and coupling stiffness inherent in FSI systems.

Numerically, finite element method (FEM) is employed, offering superior adaptability to unstructured meshes, which is a critical advantage for simulating complex geometries. This further enables two key enhancements: Firstly, high-order geometry fidelity: In this work, a second order body-fitted mesh is applied, combined with the use of isoparametric finite element function spaces, achieving precise geometric approximation of solid boundaries and enhancing spatial convergence. Second, computational efficiency: The use of finite element method provides good flexibility in mesh design and enables local mesh refinement, which could significantly reduce grid counts compared to traditional Cartesian approaches, facilitating practical three-dimensional simulations.

The paper is arranged as follows: Chapter 2 derives the FSI model based on the incompressible elastic fluid model and its variational formulation based on the ALE framework. Chapter 3 presents the high-order spatial and temporal discretization of the derived problem. Chapter 4 states a local updating algorithm that is suitable for large movement and multiscale FSI simulation. Chapter 5 validates the model through benchmark tests and provides comprehensive 2D/3D numerical demonstrations.

## 2 Arbitrary Lagrangian Eulerian (ALE) Formulation of a Sharp Interface FSI Model

In this section, we first introduce the incompressible elastic model in fluid structure interaction problem, then derive the sharp interface formulation and governing equations based on it.

### 2.1 Incompressible elastic model for fluid-structure interaction

We consider a fluid-structure interaction system consisting of an incompressible Newtonian fluid and an incompressible elastic solid. The entire computational domain is denoted by  $\Omega \subset \mathbb{R}^d$  ( $d = 2, 3$ ), which is a fixed, bounded region. At time  $t$ , the solid occupies the subdomain  $\Omega_s^t \subset \Omega$ , which is the image of the reference configuration  $\Omega_s^0$  under the deformation map  $\mathbf{X}(\cdot, t) : \Omega_s^0 \rightarrow \Omega_s^t$ . The fluid occupies the remaining part of the domain, denoted as  $\Omega_f^t = \Omega \setminus \overline{\Omega_s^t}$ . The interface between the fluid and solid is represented by  $\Gamma^t = \partial\Omega_s^t \cap \partial\Omega_f^t$ . We assume that the solid is always fully immersed in the fluid and does not contact the

external boundary, i.e.,  $\partial\Omega_s^t \cap \partial\Omega = \emptyset$  for all  $t \in [0, T]$ . Consequently, the boundary  $\partial\Omega$  of the domain  $\Omega$  is fixed and is in contact only with the fluid.

The motion of the fluid is governed by the incompressible Navier-Stokes equations:

$$\begin{cases} \frac{\partial \mathbf{u}_f}{\partial t} + (\mathbf{u}_f \cdot \nabla) \mathbf{u}_f = \nabla \cdot \boldsymbol{\sigma}_f, & \text{in } \Omega_f^t, \\ \nabla \cdot \mathbf{u}_f = 0, & \text{in } \Omega_f^t, \end{cases} \quad (1)$$

where  $\mathbf{u}_f$  denote the fluid velocity, respectively. The fluid stress tensor  $\boldsymbol{\sigma}_f$  is given by

$$\boldsymbol{\sigma}_f = -P_f I + \frac{2}{Re} \mathbf{D}(\mathbf{u}_f), \quad (2)$$

with  $\mathbf{D}(\mathbf{u}_f) = \frac{1}{2}(\nabla \mathbf{u}_f + (\nabla \mathbf{u}_f)^T)$  representing the rate-of-deformation tensor,  $P_f$  denoting the fluid pressure, and  $Re$  being the Reynolds number.

For the solid, we adopt a neo-Hookean elastic model. The solid motion is described by the following equations:

$$\begin{cases} \partial_t \mathbf{u}_s + (\mathbf{u}_s \cdot \nabla) \mathbf{u}_s = \nabla \cdot \boldsymbol{\sigma}_s, & \text{in } \Omega_s^t, \\ \nabla \cdot \mathbf{u}_s = 0, & \text{in } \Omega_s^t, \end{cases} \quad (3)$$

where  $\mathbf{u}_s = \partial_t \mathbf{X} \circ \mathbf{X}^{-1}$  is the solid velocity. The solid stress tensor  $\boldsymbol{\sigma}_s$  is defined as

$$\boldsymbol{\sigma}_s = -P_s I + \frac{E}{Re} (\mathcal{B} - I), \quad (4)$$

where  $P_s$  is the solid pressure,  $E$  is the dimensionless elastic modulus, and  $\mathcal{B} = \mathbf{F} \mathbf{F}^T$  is the left Cauchy-Green deformation tensor with  $\mathbf{F} = \nabla \mathbf{X} \mathbf{X}$  being the deformation gradient tensor. The deformation gradient  $\mathbf{F}$  evolves according to the kinematic relation [22]

$$\frac{\partial \mathbf{F}}{\partial t} + (\mathbf{u}_s \cdot \nabla) \mathbf{F} = (\nabla \mathbf{u}_s)^T \mathbf{F},$$

where we use a row-wise nabla operator, i.e.,

$$(\mathcal{B}(\nabla \mathbf{u}_s))_{ij} = \mathcal{B}_{ik} \partial_k (\mathbf{u}_s)_j.$$

This leads to the evolution equation for

$$\frac{\partial \mathcal{B}}{\partial t} + (\mathbf{u}_s \cdot \nabla) \mathcal{B} - (\nabla \mathbf{u}_s)^T \mathcal{B} - \mathcal{B}(\nabla \mathbf{u}_s) = 0,$$

which expresses the vanishing of the upper-convected time derivative of  $\mathcal{B}$ .

The fluid and solid are coupled through the following interface conditions on  $\Gamma^t$ :

$$\begin{cases} \mathbf{u}_f = \mathbf{u}_s, & \text{on } \Gamma^t, \\ \boldsymbol{\sigma}_f \mathbf{n} = \boldsymbol{\sigma}_s \mathbf{n}, & \text{on } \Gamma^t, \end{cases} \quad (5)$$

where  $\mathbf{n}$  is the unit normal vector on  $\Gamma^t$  pointing from the solid to the fluid. Since the velocities are continuous across the interface, we denote the common velocity field as  $\mathbf{u}$ . Thus, together with suitable boundary and initial conditions, the coupled FSI system is given by:

$$\left\{ \begin{array}{ll} \frac{\partial \mathbf{u}}{\partial t} + (\mathbf{u} \cdot \nabla) \mathbf{u} + \nabla P_s = \frac{E}{Re} \nabla \cdot (\mathcal{B} - I) , & \text{in } \Omega_s^t , \\ \frac{\partial \mathbf{u}}{\partial t} + (\mathbf{u} \cdot \nabla) \mathbf{u} + \nabla P_f = \frac{1}{Re} \nabla \cdot (2\mathbf{D}(\mathbf{u})) , & \text{in } \Omega_f^t , \\ \nabla \cdot \mathbf{u} = 0 , & \text{in } \Omega , \\ \frac{\partial \mathcal{B}}{\partial t} + (\mathbf{u} \cdot \nabla) \mathcal{B} - (\nabla \mathbf{u})^T \mathcal{B} - \mathcal{B} \nabla \mathbf{u} = 0 , & \text{in } \Omega_s^t , \\ \mathbf{u}_f = \mathbf{u}_s , & \text{on } \Gamma^t , \\ \boldsymbol{\sigma}_f \mathbf{n} = \boldsymbol{\sigma}_s \mathbf{n} , & \text{on } \Gamma^t , \\ \mathbf{u} = 0 , & \text{on } \partial\Omega , \\ \mathbf{u}(\mathbf{x}, 0) = \mathbf{u}_0(\mathbf{x}) , \mathcal{B}(\mathbf{x}, 0) = I , & \text{in } \Omega , \end{array} \right. \quad (6)$$

where the interface terms cancel out due to the interface conditions in (5).

## 2.2 Variational formulation and ALE mapping

Let us denote by  $H^1(\Omega)$  the Sobolev space of square-integrable functions with square-integrable first derivatives, and by  $L^2(\Omega)$  the space of square-integrable functions. We define the following function spaces:

$$\begin{aligned} \mathbf{V}^t &= \{\mathbf{v} \in H^1(\Omega)^d \mid \mathbf{v} = 0 \text{ on } \partial\Omega\} , \\ Q_s^t &= \{q^s \in L^2(\Omega_s^t) \mid \int_{\Omega_s^t} q^s d\mathbf{x} = 0\} , \\ Q_f^t &= \{q^f \in L^2(\Omega_f^t) \mid \int_{\Omega_f^t} q^f d\mathbf{x} = 0\} , \\ \mathbb{B}^t &= L^2(\Omega_s^t)^{d \times d} . \end{aligned}$$

Multiplying the momentum equations in (6) by a test function  $\mathbf{v} \in V^t$ , and integrating by part over  $\Omega_s^t$  and  $\Omega_f^t$ , we obtain:

$$\begin{aligned} & \int_{\Omega} \frac{\partial \mathbf{u}}{\partial t} \cdot \mathbf{v} d\mathbf{x} + \int_{\Omega} (\mathbf{u} \cdot \nabla) \mathbf{u} \cdot \mathbf{v} d\mathbf{x} + \frac{1}{Re} \int_{\Omega} 2\mathbf{D}(\mathbf{u}) : \mathbf{D}(\mathbf{v}) d\mathbf{x} \\ & - \int_{\Omega_s^t} P^s \nabla \cdot \mathbf{v} d\mathbf{x} - \int_{\Omega_f^t} P^f \nabla \cdot \mathbf{v} d\mathbf{x} + \frac{E}{Re} \int_{\Omega_s^t} (\mathcal{B} - I) : \nabla \mathbf{v} d\mathbf{x} \\ & = \int_{\Gamma^t} (\boldsymbol{\sigma}_s \mathbf{n}) \cdot \mathbf{v} dS - \int_{\Gamma^t} (\boldsymbol{\sigma}_f \mathbf{n}) \cdot \mathbf{v} dS = 0 . \end{aligned} \quad (7)$$

Denoting  $(\cdot, \cdot)_{\Omega}$ ,  $(\cdot, \cdot)_{\Omega_s^t}$  and  $(\cdot, \cdot)_{\Omega_f^t}$  as the  $L^2$  inner products in  $\Omega$ ,  $\Omega_s^t$  and  $\Omega_f^t$  respectively, the weak formulation of the FSI model is to find  $(\mathbf{u}, P^s, P^f, \mathcal{B}) \in \mathbf{V}^t \times Q_s^t \times Q_f^t \times \mathbb{B}^t$  such that for all  $(\mathbf{v}, q^s, q^f, \mathcal{W}) \in$

$$\mathbf{V}^t \times Q_s^t \times Q_f^t \times \mathbb{B}^t$$

$$\left\{ \begin{array}{l} \left( \frac{\partial \mathbf{u}}{\partial t}, \mathbf{v} \right)_\Omega + ((\mathbf{u} \cdot \nabla) \mathbf{u}, \mathbf{v})_\Omega + \frac{1}{Re} (2\mathbf{D}(\mathbf{u}), \mathbf{D}(\mathbf{v}))_{\Omega_f} \\ \quad - (P^s, \nabla \cdot \mathbf{v})_{\Omega_s^t} - (P^f, \nabla \cdot \mathbf{v})_{\Omega_f^t} + \frac{E}{Re} ((\mathcal{B} - \mathbf{I}), \nabla \mathbf{v})_{\Omega_s^t} = 0, \\ (\nabla \cdot \mathbf{u}, q^s)_{\Omega_s^t} = 0, \\ (\nabla \cdot \mathbf{u}, q^f)_{\Omega_f^t} = 0, \\ \left( \frac{\partial \mathcal{B}}{\partial t}, \mathcal{W} \right)_{\Omega_s^t} + ((\mathbf{u} \cdot \nabla) \mathcal{B}, \mathcal{W})_{\Omega_s^t} - ((\nabla \mathbf{u})^T \mathcal{B}, \mathcal{W})_{\Omega_s^t} - (\mathcal{B} \nabla \mathbf{u}, \mathcal{W})_{\Omega_s^t} = 0. \end{array} \right. \quad (8)$$

Although the weak formulation (8) is straightforward, the time-dependent domains  $\Omega_s^t$  and  $\Omega_f^t$  introduce significant complexity in numerical discretization. To address this, we employ an ALE framework to map all variables back to a fixed reference domain  $\Omega$ , simplifying the temporal discretization process. We introduce the following mapping:

$$\mathcal{A}(\mathbf{x}, t) : \Omega \times [0, T] \rightarrow \Omega, \quad \mathbf{x} \in \Omega, \quad t \in [0, T]. \quad (9)$$

The mapping should satisfy  $\mathcal{A}(\mathbf{x}, 0) = \mathbf{x}$  and  $\mathcal{A}(\Omega_s^0, t) = \Omega_s^t$ . We also introduce the mesh velocity  $w(\mathcal{A}(\mathbf{x}, t), t) = \frac{\partial \mathcal{A}(\mathbf{x}, t)}{\partial t}$  to construct the mapping through solving a harmonic extension problem

$$\left\{ \begin{array}{ll} \Delta w = 0, & \text{in } \Omega_f^t, \\ w = \mathbf{u}, & \text{in } \Omega_s^t, \\ w = 0, & \text{on } \partial\Omega. \end{array} \right. \quad (10)$$

Then all of the variables could be pulled back to the reference configuration. We denote  $\hat{\mathbf{u}}(\mathbf{x}, t) = \mathbf{u}(\mathcal{A}(\mathbf{x}, t), t)$ ,  $\hat{P}^s(\mathbf{x}, t) = P^s(\mathcal{A}(\mathbf{x}, t), t)$ ,  $\hat{P}^f(\mathbf{x}, t) = P^f(\mathcal{A}(\mathbf{x}, t), t)$ ,  $\hat{\mathcal{B}}(\mathbf{x}, t) = \mathcal{B}(\mathcal{A}(\mathbf{x}, t), t)$ ,  $\hat{w}_t(\mathbf{x}, t) = w_t(\mathcal{A}(\mathbf{x}, t), t)$ . Moreover, we introduce some notations in the reference configuration:

$$\hat{J} = |\det(\frac{\partial \mathcal{A}}{\partial \mathbf{x}})|, \quad \hat{\mathbf{F}} = \frac{\partial \mathcal{A}}{\partial \mathbf{x}}, \quad \hat{\mathbf{F}}^{-1} = (\frac{\partial \mathcal{A}}{\partial \mathbf{x}})^{-1}, \quad \hat{\nabla} = \frac{\partial}{\partial \mathbf{x}}, \quad \hat{D}(\cdot) = \frac{1}{2}(\hat{\nabla}(\cdot) \hat{\mathbf{F}}^{-1} + \hat{\mathbf{F}}^{-T}(\hat{\nabla}(\cdot))^T). \quad (11)$$

Then the weak formulation (8) could be rewritten into the reference configuration as: find  $(\hat{\mathbf{u}}, \hat{P}^s, \hat{P}^f, \hat{\mathcal{B}}, \hat{w}) \in$

$\mathbf{V}^0 \times Q_s^0 \times Q_f^0 \times \mathbb{B}^0 \times \mathbf{V}^0$  such that for all  $(\hat{\mathbf{v}}, \hat{q}^s, \hat{q}^f, \hat{\mathcal{W}}, \hat{v}) \in \mathbf{V}^0 \times Q_s^0 \times Q_f^0 \times \mathbb{B}^0 \times \mathbf{V}^0$

$$\left\{ \begin{array}{l} (\hat{J} \frac{\partial \hat{\mathbf{u}}}{\partial t}, \hat{\mathbf{v}})_\Omega + (\hat{J}(\hat{\mathbf{u}} - \hat{w}) \cdot \hat{\nabla} \hat{\mathbf{u}} \hat{\mathbf{F}}^{-1}, \hat{\mathbf{v}})_\Omega + \frac{1}{Re} (\hat{J} 2 \hat{D}(\hat{\mathbf{u}}) \hat{\mathbf{F}}^{-T}, \hat{D}(\hat{\mathbf{v}}) \hat{\mathbf{F}}^{-T})_{\Omega_f^0} \\ \quad - (\hat{J} \hat{P}^s, \text{tr}(\hat{\nabla} \hat{\mathbf{v}} \hat{\mathbf{F}}^{-1}))_{\Omega_s^0} - (\hat{J} \hat{P}^f, \text{tr}(\hat{\nabla} \hat{\mathbf{v}} \hat{\mathbf{F}}^{-1}))_{\Omega_f^0} + \frac{E}{Re} (\hat{J}(\hat{\mathcal{B}} - \mathbf{I}), \hat{\nabla}(\hat{\mathbf{v}}) \hat{\mathbf{F}}^{-1})_{\Omega_s^0} = 0, \\ (\hat{J} \text{tr}(\hat{\nabla} \hat{\mathbf{u}} \hat{\mathbf{F}}^{-1}), \hat{q}^s)_{\Omega_s^0} = 0, \\ (\hat{J} \text{tr}(\hat{\nabla} \hat{\mathbf{u}} \hat{\mathbf{F}}^{-1}), \hat{q}^f)_{\Omega_f^0} = 0, \\ (\hat{J} \frac{\partial \hat{\mathcal{B}}}{\partial t}, \hat{\mathcal{W}})_{\Omega_s^0} + (\hat{J}(\hat{\mathbf{u}} - \hat{w}) \cdot \hat{\nabla} \hat{\mathcal{B}} \hat{\mathbf{F}}^{-1}, \hat{\mathcal{W}})_{\Omega_s^0} - (\hat{J}(\hat{\nabla} \hat{\mathbf{u}} \hat{\mathbf{F}}^{-1})^T \hat{\mathcal{B}}, \hat{\mathcal{W}})_{\Omega_s^0} - (\hat{J} \hat{\mathcal{B}} \hat{\nabla} \hat{\mathbf{u}} \hat{\mathbf{F}}^{-1}, \hat{\mathcal{W}})_{\Omega_s^0} = 0, \\ (\hat{\nabla} \hat{w}, \hat{\nabla} \hat{v})_\Omega = 0, \\ \hat{w} = \hat{\mathbf{u}}, \quad \text{in } \Omega_s^0, \\ \hat{w} = 0, \quad \text{on } \partial\Omega, \\ \frac{\partial \mathcal{A}(\mathbf{x}, t)}{\partial t} = \hat{w}(\mathbf{x}, t), \quad \mathcal{A}(\mathbf{x}, 0) = \mathbf{x} \quad \text{in } \Omega. \end{array} \right. \quad (12)$$

### 3 Discretization

Let  $\mathcal{T}_h$  be a fitted triangulation of the reference domain  $\Omega$  (the initial configuration at  $t = 0$ ) with mesh size  $h$ , which conforms to the initial fluid-structure interface  $\Gamma^0 = \partial\Omega_s^0 \cap \partial\Omega_f^0$ .

For spatial discretization, we adopt the classical Taylor-Hood  $\mathcal{P}_2/\mathcal{P}_1$  finite element pair for velocity-pressure approximation, and  $\mathcal{P}_1$  elements for the left Cauchy-Green tensor  $\mathcal{B}$ . Let  $\hat{K}$  denote a reference simplex (triangle in 2D or tetrahedron in 3D), and let  $\mathcal{P}_k(\hat{K})$  be the space of polynomials of total degree at most  $k$  on  $\hat{K}$ .

For the discrete approximation of the ALE mapping, we define  $\mathcal{A}_h : \Omega \times [0, T] \rightarrow \mathbb{R}^d$  that is constructed using finite element basis functions. Specifically, at each time  $t$ ,  $\mathcal{A}_{h,t} = \mathcal{A}_h(\cdot, t)$  is a piecewise polynomial map that moves the mesh nodes in a way that approximates the continuous motion. The discrete domain at time  $t$  is then defined as

$$\Omega_h(t) = \mathcal{A}_{h,t}(\Omega) = \Omega_{s,h}^t \cup \Omega_{f,h}^t \cup \Gamma_h^t,$$

where  $\Omega_{s,h}^t = \mathcal{A}_{h,t}(\Omega_s^0)$  and  $\Omega_{f,h}^t = \mathcal{A}_{h,t}(\Omega_f^0)$  are approximations to the true solid and fluid domains, respectively. The discrete interface  $\Gamma_h^t = \partial\Omega_{s,h}^t \cap \partial\Omega_{f,h}^t$  approximates the true interface  $\Gamma^t$ . We also use the similar notations with subscript  $h$  to denote the discrete ALE mapping related quantities, e.g.,  $\hat{\mathbf{F}}_h = \frac{\partial \mathcal{A}_h}{\partial \mathbf{x}}$ ,  $\hat{J}_h = |\det(\hat{\mathbf{F}}_h)|$ , etc. We shall use the same element for velocity to approximate the ALE mapping  $\mathcal{A}_h$ .

The finite element spaces on the reference domain  $\Omega$  are defined as:

$$\begin{aligned} \hat{\mathbf{V}}_h &= \left\{ \hat{\mathbf{v}}_h \in \mathbf{H}^1(\Omega) : \hat{\mathbf{v}}_h|_K \circ F_K^{-1} \in [\mathcal{P}_2(\hat{K})]^d, \forall K \in \mathcal{T}_h \right\}, \\ \hat{Q}_{s,h} &= \left\{ \hat{q}_h^s \in L^2(\Omega_s^0) : \hat{q}_h^s|_K \circ F_K^{-1} \in \mathcal{P}_1(\hat{K}), \forall K \in \mathcal{T}_h, K \subset \Omega_s^0 \right\}, \\ \hat{Q}_{f,h} &= \left\{ \hat{q}_h^f \in L^2(\Omega_f^0) : \hat{q}_h^f|_K \circ F_K^{-1} \in \mathcal{P}_1(\hat{K}), \forall K \in \mathcal{T}_h, K \subset \Omega_f^0 \right\}, \\ \hat{\mathbf{B}}_h &= \left\{ \hat{\mathbf{B}}_h \in [L^2(\Omega_s^0)]^{d \times d} : \hat{\mathbf{B}}_h|_K \circ F_K^{-1} \in [\mathcal{P}_1(\hat{K})]^{d \times d}, \forall K \in \mathcal{T}_h, K \subset \Omega_s^0 \right\}, \end{aligned}$$

where  $F_K : \hat{K} \rightarrow K$  is the isoparametric mapping from the reference element to each physical element  $K$  in the reference mesh.

**Remark 1.** By employing isoparametric elements, the second-order geometric approximation remains consistent with the finite element spaces, thereby minimizing boundary errors and preserving high-order spatial convergence for the FSI model.

The space discretized problem is to find  $(\hat{\mathbf{u}}_h, \hat{P}_h^s, \hat{P}_h^f, \hat{\mathcal{B}}_h, \hat{w}_{t,h}) \in \hat{V}_h \times \hat{Q}_{s,h} \times \hat{Q}_{f,h} \times \hat{\mathbb{B}}_h \times \hat{V}_h$  such that for all  $(\hat{\mathbf{v}}_h, \hat{q}_h^s, \hat{q}_h^f, \hat{\mathcal{W}}_h, \hat{v}_h) \in \hat{V}_h \times \hat{Q}_{s,h} \times \hat{Q}_{f,h} \times \hat{\mathbb{B}}_h \times \hat{V}_h$

$$\left\{ \begin{array}{l} (\hat{J}_h \frac{\partial \hat{\mathbf{u}}_h}{\partial t}, \hat{\mathbf{v}}_h)_\Omega + (\hat{J}_h (\hat{\mathbf{u}}_h - \hat{w}_h) \cdot \hat{\nabla} \hat{\mathbf{u}}_h \hat{\mathbf{F}}_h^{-1}, \hat{\mathbf{v}}_h)_\Omega + \frac{1}{Re} (\hat{J}_h 2\hat{D}(\hat{\mathbf{u}}_h), \hat{D}(\hat{\mathbf{v}}_h))_{\Omega_f^0} \\ \quad - (\hat{J}_h \hat{P}_h^s, \text{tr}(\hat{\nabla} \hat{\mathbf{v}}_h \hat{\mathbf{F}}_h^{-1}))_{\Omega_s^0} - (\hat{J}_h \hat{P}_h^f, \text{tr}(\hat{\nabla} \hat{\mathbf{v}}_h \hat{\mathbf{F}}_h^{-1}))_{\Omega_f^0} + \frac{E}{Re} (\hat{J}_h (\hat{\mathcal{B}}_h - \mathbf{I}), \hat{\nabla}(\hat{\mathbf{v}}_h) \hat{\mathbf{F}}_h^{-1})_{\Omega_s^0} = 0, \\ (\hat{J}_h \text{tr}(\hat{\nabla} \hat{\mathbf{u}}_h \hat{\mathbf{F}}_h^{-1}), \hat{q}_h^s)_{\Omega_s^0} = 0, \\ (\hat{J}_h \text{tr}(\hat{\nabla} \hat{\mathbf{u}}_h \hat{\mathbf{F}}_h^{-1}), \hat{q}_h^f)_{\Omega_f^0} = 0, \\ (\hat{J}_h \frac{\partial \hat{\mathcal{B}}_h}{\partial t}, \hat{\mathcal{W}}_h)_{\Omega_s^0} + (\hat{J}_h (\hat{\mathbf{u}}_h - \hat{w}_h) \cdot \hat{\nabla} \hat{\mathcal{B}}_h \hat{\mathbf{F}}_h^{-1}, \hat{\mathcal{W}}_h)_{\Omega_s^0} - (\hat{J}_h (\hat{\nabla} \hat{\mathbf{u}}_h \hat{\mathbf{F}}_h^{-1})^T \hat{\mathcal{B}}_h, \hat{\mathcal{W}}_h)_{\Omega_s^0} - (\hat{J}_h \hat{\mathcal{B}}_h \hat{\nabla} \hat{\mathbf{u}}_h \hat{\mathbf{F}}_h^{-1}, \hat{\mathcal{W}}_h)_{\Omega_s^0} = 0, \\ (\hat{\nabla} \hat{w}_h, \hat{\nabla} \hat{v}_h)_\Omega = 0, \\ \hat{w}_h = \hat{\mathbf{u}}_h, \\ \hat{w}_h = 0, \\ \frac{\partial \mathcal{A}_h(\mathbf{x}, t)}{\partial t} = \hat{w}_h(\mathbf{x}, t), \quad \mathcal{A}_h(\mathbf{x}, 0) = \mathbf{x} \end{array} \right. \quad \begin{array}{l} \text{in } \Omega_s^0, \\ \text{on } \partial\Omega, \\ \text{in } \Omega, \end{array}$$

Now all of the variables are defined on the fixed reference domain, and we can perform the time discretization directly. We use a partitioned Runge-Kutta method for time discretization. For notational simplicity and algorithmic clarity, we recast the coupled system (13) into the compact abstract form (14) by introducing the composite solution vector  $\mathbf{X} = (\hat{\mathbf{u}}_h, \hat{P}_h^s, \hat{P}_h^f, \hat{\mathcal{B}}_h)$ , test function vector  $\Phi = (\hat{\mathbf{v}}_h, \hat{q}_h^s, \hat{q}_h^f, \hat{\mathcal{W}}_h)$ , the composite function space  $\mathcal{X}_h = \hat{V}_h \times \hat{Q}_{s,h} \times \hat{Q}_{f,h} \times \hat{\mathbb{B}}_h$ , and the nonlinear operator  $\mathcal{F}$  encapsulating the weak form of the governing equations:

$$\begin{aligned} \mathcal{F}(\partial_t \mathbf{X}_h, \mathbf{X}_h; \Phi; \mathcal{A}_h, w_h) &= 0, \quad \text{for all } \Phi \in \mathcal{X}_h, \\ (\nabla w_h, \nabla v_h)_\Omega &= 0, \quad \text{for all } v_h \in \hat{V}_h, \\ \hat{w}_h &= \hat{\mathbf{u}}_h, \quad \text{in } \Omega_s^0, \\ \partial_t \mathcal{A}_h &= \hat{w}_h, \quad \text{in } \Omega, \\ \mathcal{A}_h(\mathbf{x}, 0) &= \mathbf{x}, \quad \text{in } \Omega, \end{aligned} \quad (14)$$

where  $\mathcal{F}$  is defined by

$$\begin{aligned} \mathcal{F}(\partial_t \mathbf{X}_h, \mathbf{X}_h; \Phi; \mathcal{A}_h, w_h) &= (\hat{J}_h \partial_t \hat{\mathbf{u}}_h, \hat{\mathbf{v}}_h)_\Omega + (\hat{J}_h (\hat{\mathbf{u}}_h - \hat{w}_h) \cdot \hat{\nabla} \hat{\mathbf{u}}_h \hat{\mathbf{F}}_h^{-1}, \hat{\mathbf{v}}_h)_\Omega + \frac{1}{Re} (\hat{J}_h 2\hat{D}(\hat{\mathbf{u}}_h), \hat{D}(\hat{\mathbf{v}}_h))_{\Omega_f^0} \\ &\quad - (\hat{J}_h \hat{P}_h^s, \text{tr}(\hat{\nabla} \hat{\mathbf{v}}_h \hat{\mathbf{F}}_h^{-1}))_{\Omega_s^0} - (\hat{J}_h \hat{P}_h^f, \text{tr}(\hat{\nabla} \hat{\mathbf{v}}_h \hat{\mathbf{F}}_h^{-1}))_{\Omega_f^0} + \frac{E}{Re} (\hat{J}_h (\hat{\mathcal{B}}_h - \mathbf{I}), \hat{\nabla}(\hat{\mathbf{v}}_h) \hat{\mathbf{F}}_h^{-1})_{\Omega_s^0} \\ &\quad + (\hat{J}_h \text{tr}(\hat{\nabla} \hat{\mathbf{u}}_h \hat{\mathbf{F}}_h^{-1}), \hat{q}_h^s)_{\Omega_s^0} + (\hat{J}_h \text{tr}(\hat{\nabla} \hat{\mathbf{u}}_h \hat{\mathbf{F}}_h^{-1}), \hat{q}_h^f)_{\Omega_f^0} \\ &\quad + (\hat{J}_h \partial_t \hat{\mathcal{B}}_h, \hat{\mathcal{W}}_h)_{\Omega_s^0} + (\hat{J}_h (\hat{\mathbf{u}}_h - \hat{w}_h) \cdot \hat{\nabla} \hat{\mathcal{B}}_h \hat{\mathbf{F}}_h^{-1}, \hat{\mathcal{W}}_h)_{\Omega_s^0} \\ &\quad - (\hat{J}_h (\hat{\nabla} \hat{\mathbf{u}}_h \hat{\mathbf{F}}_h^{-1})^T \hat{\mathcal{B}}_h, \hat{\mathcal{W}}_h)_{\Omega_s^0} - (\hat{J}_h \hat{\mathcal{B}}_h \hat{\nabla} \hat{\mathbf{u}}_h \hat{\mathbf{F}}_h^{-1}, \hat{\mathcal{W}}_h)_{\Omega_s^0}. \end{aligned} \quad (15)$$

We now proceed to discretize (14) in time using a semi-implicit Euler scheme. The idea is to set up a partitioned Runge-Kutta method [2, 18] where the mesh motion is solved separately from the main FSI

system at each time step. Let  $t_n = n\Delta t$  for  $n = 0, 1, 2, \dots, N$  denote the discrete time levels with uniform step size  $\Delta t$ . The time derivative is approximated as:

$$\partial_t \mathbf{X}_h^{n+1} \approx \frac{\mathbf{X}_h^{n+1} - \mathbf{X}_h^n}{\Delta t}, \quad \partial_t \mathcal{A}_h^{n+1} \approx \frac{\mathcal{A}_h^{n+1} - \mathcal{A}_h^n}{\Delta t}. \quad (16)$$

Then the discretisation scheme for (14) reads:

Step 1: Given  $\mathbf{X}_h^n$  and  $\mathcal{A}_h^n$ , find  $\mathbf{X}_h^{n+1}$  such that for all  $\Phi \in \mathcal{X}_h$

$$\mathcal{F}\left(\frac{\mathbf{X}_h^{n+1} - \mathbf{X}_h^n}{\Delta t}, \mathbf{X}_h^{n+1}; \Phi; \mathcal{A}_h^n, w_{t,h}^n\right) = 0, \quad \text{in } \Omega. \quad (17)$$

Step 2: Find  $w_{t,h}^{n+1}$  such that for all  $v_h \in \hat{V}_h$

$$\begin{aligned} (\nabla w_{t,h}^{n+1}, \nabla v_h)_\Omega &= 0, & \text{for all } v_h \in \hat{V}_h, \\ w_{t,h}^{n+1} &= \mathbf{u}_h^{n+1}, & \text{in } \Omega_s^0, \\ w_{t,h}^{n+1} &= 0, & \text{on } \partial\Omega. \end{aligned} \quad (18)$$

Step 3: Update the mapping  $\mathcal{A}_h^{n+1}$  by

$$\mathcal{A}_h^{n+1} = \mathcal{A}_h^n + \Delta t w_{t,h}^{n+1}. \quad (19)$$

Step 4: Time step  $n = n + 1$  and go to step 1 until  $n = N$ .

We also show the second order time discretisation scheme as follows. Let  $\gamma = 1 - \frac{1}{\sqrt{2}}$ ,  $\beta_0 = -\sqrt{2}$ ,  $\beta_* = 1 + \sqrt{2}$ ,  $c_0 = -\frac{1}{\sqrt{2}}$ ,  $c_* = 1 + \frac{1}{\sqrt{2}}$ , the second order time discretisation scheme reads:

Step 1: Given  $\mathbf{X}_h^n$ , find  $w_{t,h}^{n*}$  such that for all  $v_h \in \hat{V}_h$

$$\begin{aligned} (\nabla w_{t,h}^{n*}, \nabla v_h)_\Omega &= 0, & \text{for all } v_h \in \hat{V}_h, \\ w_{t,h}^{n*} &= \mathbf{u}_h^n, & \text{in } \Omega_s^0, \\ w_{t,h}^{n*} &= 0, & \text{on } \partial\Omega. \end{aligned} \quad (20)$$

Step 2: Update the mapping  $\mathcal{A}_h^{n*}$  by

$$\mathcal{A}_h^{n*} = \mathcal{A}_h^n + \gamma \Delta t w_{t,h}^{n*}. \quad (21)$$

Step 3: Find  $\mathbf{X}_h^{n*}$  such that for all  $\Phi \in \mathcal{X}_h$

$$\mathcal{F}\left(\frac{\mathbf{X}_h^{n*} - \mathbf{X}_h^n}{\gamma \Delta t}, \mathbf{X}_h^{n*}; \Phi; \mathcal{A}_h^{n*}, w_{t,h}^{n*}\right) = 0, \quad \text{for all } \Phi \in \mathcal{X}_h. \quad (22)$$

Step 4: Find  $w_{t,h}^{n+1}$  such that for all  $v_h \in \hat{V}_h$

$$\begin{aligned} (\nabla w_{t,h}^{n+1}, \nabla v_h)_\Omega &= 0, & \text{for all } v_h \in \hat{V}_h, \\ w_{t,h}^{n+1} &= c_0 \mathbf{u}_h^n + c_* \mathbf{u}_h^{n*}, & \text{in } \Omega_s^0, \\ w_{t,h}^{n+1} &= 0, & \text{on } \partial\Omega. \end{aligned} \quad (23)$$

Step 5: Update the mapping  $\mathcal{A}_h^{n+1}$  by

$$\mathcal{A}_h^{n+1} = \mathcal{A}_h^n + \Delta t w_{t,h}^{n+1}. \quad (24)$$

Step 6: Find  $\mathbf{X}_h^{n+1}$  such that for all  $\Phi \in \mathcal{X}_h$

$$\mathcal{F}\left(\frac{\mathbf{X}_h^{n+1} - \beta_0 \mathbf{X}_h^n - \beta_* \mathbf{X}_h^*}{\gamma \Delta t}, \mathbf{X}_h^{n+1}; \Phi; \mathcal{A}^{n+1}, w_{t,h}^{n+1}\right) = 0, \quad \text{for all } \Phi \in \mathcal{X}_h. \quad (25)$$

Step 7: Time step  $n = n + 1$  and go to step 1 until  $n = N$ .

## 4 Local Updating Algorithm for Multi-scale Simulation

This chapter introduces the implementation of the numerical algorithm. Due to the high complexity of the three-dimensional simulation and the large number of unknowns in the aforementioned model, directly solving the fluid-structure interaction (FSI) equations over a large flow domain is computationally prohibitive. Moreover, in many practical applications, the need of simulating a long-distance transport of particles within asymmetric flow fields is general, such as particle focusing [33] and related phenomena. To address this, a localized updating strategy is developed.

In practical scenarios, the size of the solid body (e.g., a small sphere) and the length of the flow channel span multiple scales, while the Reynolds number remains low. Thus, in regions far from the sphere, the flow field can be assumed as a steady laminar flow unaffected by the sphere's motion. The algorithm proceeds as follows:

Step 1: Construct a background mesh  $M_{bg}$  for the entire flow channel. Create finite element spaces  $V_{bg} \times Q_{bg}^f$  on  $M_{bg}$ , define  $(\mathbf{u}_{bg}, P_{bg}) \in V_{bg} \times Q_{bg}^f$ . Then, solve the Navier-Stokes equations with a certain inflow boundary condition to obtain the background velocity  $\mathbf{u}_{bg}$ . Ensure sufficient time steps are computed to reach a stabilized flow field.

Step 2: Generate a body-fitted local mesh  $M_{local}$  around the current position of the sphere. Create finite element spaces  $V_{local}, Q_{local}^s, Q_{local}^f, \mathbf{B}_{local}$  on  $M_{local}$ . Define functions  $(\mathbf{u}_{local}^n, P_{local}^{s,n}, P_{local}^{f,n}, \mathcal{B}_{local}^n)$  and  $(\mathbf{u}_{local}^{n+1}, P_{local}^{s,n+1}, P_{local}^{f,n+1}, \mathcal{B}_{local}^{n+1}) \in V_{local} \times Q_{local}^s \times Q_{local}^f \times \mathbf{B}_{local}$ ,  $w_t^n, w_t^{n+1}$  and  $u_\Gamma \in V_{local}$ . Initialize functions  $\mathbf{u}_{local}^n, P_{local}^{s,n}, P_{local}^{f,n}, \mathcal{B}_{local}^n, w_t^n$  with property values.

Step 3: Interpolate the steady background velocity  $\mathbf{u}_{bg}$  onto  $\mathbf{u}_\Gamma$  of  $M_{local}$ .

Step 4: Solve the coupled FSI equations with Newton method mentioned in the last chapter to get the value  $(\mathbf{u}_{local}^{n+1}, P_{local}^{s,n+1}, P_{local}^{f,n+1}, \mathcal{B}_{local}^{n+1})$  of the  $(n+1)th$  time step with boundary condition  $\mathbf{u}_{local}^{n+1} = \mathbf{u}_\Gamma$  on the boundary of  $M_{local}$ .

Step 5: Compute the mesh motion velocity  $w_t^{n+1}$  based on  $\mathbf{u}_{local}^{n+1}$ . Update the sphere's position via  $x_{local}^{n+1} = x_{local}^n + w_t^{n+1} \times \Delta t$ . Where  $x_{local}^n$  and  $x_{local}^{n+1}$  means the coordinate of the mesh nodes.

Step 6: Check the updated sphere position and mesh quality. If the sphere displacement and the mesh deformation don't exceed the threshold: Set  $\mathbf{u}_{local}^n = \mathbf{u}_{local}^{n+1}, P_{local}^{s,n} = P_{local}^{s,n+1}, P_{local}^{f,n} = P_{local}^{f,n+1}, \mathcal{B}_{local}^n = \mathcal{B}_{local}^{n+1}, w_t^n = w_t^{n+1}, n = n + 1$ , and return to Step 4. Otherwise: Generate a new body-fitted mesh  $M_{local}^*$  around the updated sphere position. Create finite element spaces  $V_{local}^*, Q_{local}^{s*}, Q_{local}^{f*}, \mathbf{B}_{local}^*$  on  $M_{local}^*$ . Define functions  $(\mathbf{u}_{local}^{*n}, P_{local}^{s*,n}, P_{local}^{f*,n}, \mathcal{B}_{local}^{*n})$  and  $(\mathbf{u}_{local}^{*n+1}, P_{local}^{s*,n+1}, P_{local}^{f*,n+1}, \mathcal{B}_{local}^{*n+1}) \in V_{local}^* \times Q_{local}^{s*} \times Q_{local}^{f*} \times \mathbf{B}_{local}^*$ ,  $w_t^{*n}, w_t^{*n+1}$  and  $u_{\Gamma}^* \in V_{local}^*$ . Then, interpolate  $\mathbf{u}_{local}^{n+1}, \mathcal{B}_{local}^{n+1}$  and  $w_t^{n+1}$  from the old mesh  $M_{local}$  to  $\mathbf{u}_{local}^{*n+1}, \mathcal{B}_{local}^{*n+1}$  and  $w_t^{*n+1}$  on the overlapping regions of  $M_{local}^*$ . For non-overlapping regions, interpolate the background flow field  $\mathbf{u}_{bg}$  onto  $\mathbf{u}_{local}^{*n+1}$ . Note that When generating the new local mesh, the velocity field  $\mathbf{u}_{local}^{*n+1}$  in non-overlapping regions is directly populated using the precomputed steady background flow  $\mathbf{u}_{bg}$ . This ensures continuity of the velocity field while avoiding redundant computations in regions unaffected by the sphere's motion. For the rest of the variables, we just keep them a zero value in non-overlapping area since they don't affect the calculation.

Step 7: Dismiss the \* in all the entities defined on the new mesh  $M_{local}^*$  and proceed to Step 3.

**Remark 2.** *The localized updating strategy significantly reduces computational costs by focusing resolution near the sphere and leveraging the steady background flow elsewhere. Interpolation ensures continuity of the flow field during mesh transitions, maintaining numerical stability. This approach is demonstrated for a 2D case involving a rigid sphere in a long channel but is extensible to 3D scenarios with appropriate mesh adaptation techniques.*

Figure 1 demonstrates how the velocity field is updated and how the mesh changes throughout the algorithm. Also, Second-order elements were employed to enhance the geometric fidelity in approximating curved boundaries of solid structures, as depicted in Figure 2.

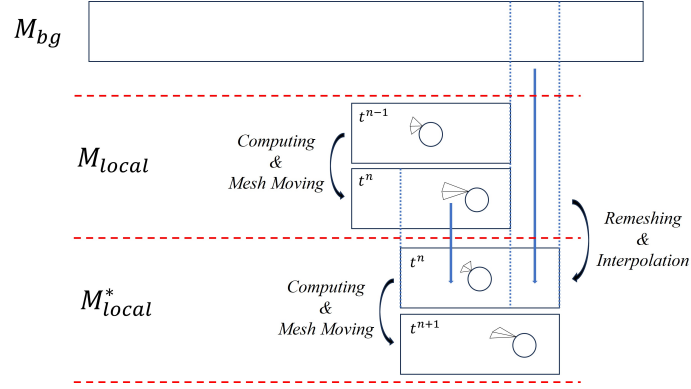


Figure 1: The figure illustrates the dynamic evolution of local mesh configurations across time steps, as well as the process of generating new meshes and interpolating field variables from the outdated mesh to the newly refined mesh when mesh quality metrics exceed predefined thresholds, thereby enabling continuous computational progression

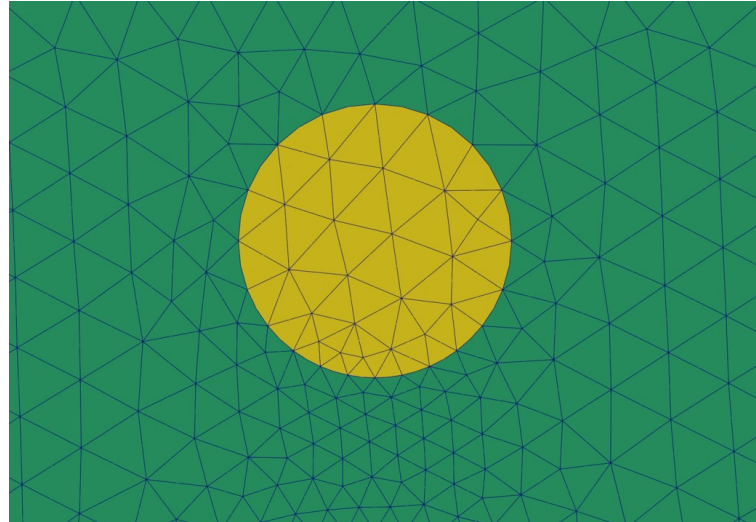


Figure 2: The second-ordered mesh fitting the boundary of the solid. The green elements represent the fluid phase while the yellow ones stand for solid phase. Notably, due to the application of high-order meshes, the elements at the fluid-solid interface adopt curved edges rather than straight edges. Unlike visualization representations, during finite element integration procedures, these curved edges are approximated using high-order polynomials, thereby better capturing curvature-induced geometric characteristics and achieving enhanced convergence rates in velocity fields.

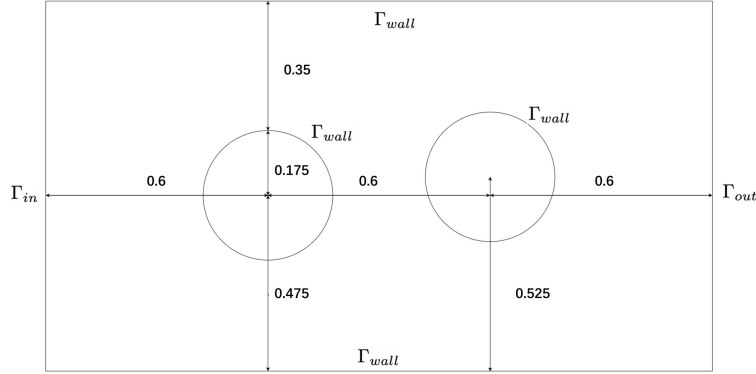


Figure 3: The domain set up for convergence study.

## 5 Numerical Results

In this chapter, we demonstrate the numerical results. Benchmarks are given to show the feasibility of the model. 2D and 3D cases are shown.

### 5.1 Convergence study by double-pillar channel flow

As illustrated in Figure 3, we first design the following test case to verify the convergence of our algorithm. The calculation domain is set to be rectangular with width  $W = 1$  and length  $L = 1.8$ . Inside the domain, two disk regions are cut to represent the pillars.

A spherical particle with radius  $r = 0.08$  is released from rest at  $(0.60, 0.76)$ , while a parabolic inflow is imposed from left to right. The inflow boundary condition is set as

$$\mathbf{u} = 0.5u_0 \frac{y(W-y)}{W^2} \mathbf{e}_x . \quad (26)$$

The corresponding parameter values are summarized below:

$$Re = 3 , E = 10^9 , u_0 = 8 . \quad (27)$$

Here, we employ a larger modulus to make the particle motion closer to that of a rigid body, thereby reducing the factors that may affect the order of convergence. Figure 4 presents the magnitude of the velocity field at a representative time instant in the simulation.

For a prescribed total simulation time, we record the trajectory of the particle's centroid throughout the whole process, as shown in Figure 5.

Apparently, the resulted particle trajectories vary under different mesh resolutions and time step sizes. This discrepancy reaches its maximum when the particle passes through the region between the two pillars, as illustrated in Figure 5. Since the largest difference of the trajectory occurs on y axis, We use the vertical coordinate as the quantity for evaluating the error. Thus the error is calculated as follows:

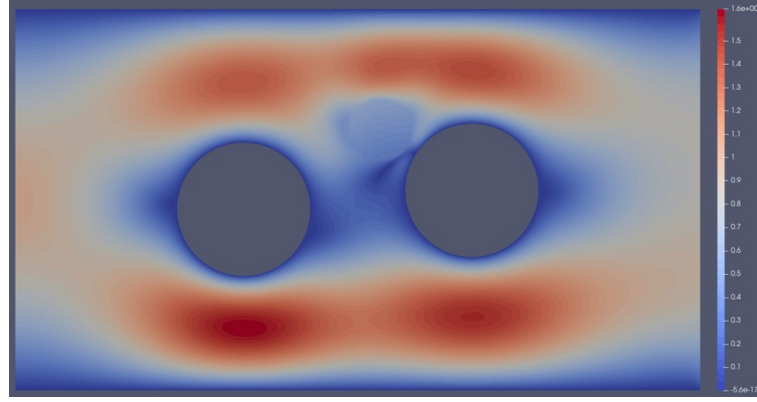


Figure 4: Magnitude of the resulted velocity field of FSI simulation. The particle of large modulus could affect the velocity field near the pillars when the distance is small.

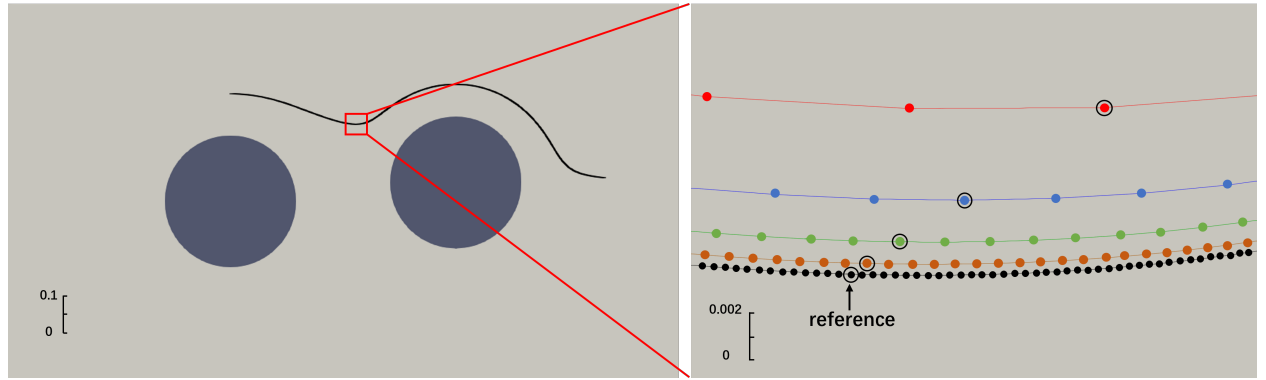


Figure 5: The figure presents the numerically computed trajectory of the center of the rigid particle. The enlarged view shows the detail of the trajectories obtained with a mesh size of  $4/100$  and time-step sizes of  $3/200$  (red),  $3/400$  (blue),  $3/800$  (green),  $3/1600$  (brown) and  $3/3200$  (black) respectively. The particle positions at different time steps are marked by points along the curves. In particular, the point enclosed by the circle indicates the particle's position at time  $t=0.375$ . For the convergence study, the particle position at this time is used to compute the numerical errors, where the solution obtained with the smallest time step ( $dt = 3/3200$ ) is taken as the reference.

$$\mathcal{E}(h) = \max_{t \in [0, T]} |\mathbf{y}_h(t) - \mathbf{y}_{\text{ref}}(t)| . \quad (28)$$

Where  $\mathbf{y}_h(t)$  and  $\mathbf{y}_{\text{ref}}(t)$  stand for the vertical coordinate of the centroid of the particle on measured trajectory and reference trajectory at the same time. The convergence rate is calculated by:

$$r_k = \frac{\ln (\mathcal{E}(h_k)/\mathcal{E}(h_{k+1}))}{\ln (h_k/h_{k+1})} . \quad (29)$$

We first examined the convergence rates of the first-order time integration scheme, which is the normal general time updating scheme, and the second-order Runge–Kutta scheme as mentioned in section 4. The results are shown in Table 1 and 2. The reference of each cases is chosen to be the trajectory received with  $dt = 3/3200$ .

Table 1: Convergence study of first-order scheme

time step	error	convergence rate
3/200	6.9e-2	
3/400	3.1e-2	1.15
3/800	1.3e-2	1.25
3/1600	4.4e-3	1.56

Table 2: Convergence study of second-order Runge–Kutta scheme

time step	error	convergence rate
3/200	4.5e-2	
3/400	1.1e-2	2.03
3/800	2.8e-3	1.97
3/1600	6.1e-4	2.20

As can be seen, the convergence rate is clear and consistent with expectations. Runge–Kutta schemes reached second order while general time updating scheme is only first-ordered.

Setting the time step size to  $dt = 3/800$ , We compare the convergence rate of first ordered mesh and second ordered mesh to show the advantage of isoparametric finite element. The corresponding results are summarized in Table 3 and Table 4. The reference of each cases are chosen to be the trajectory calculated with mesh size to be  $1/100$ .

Table 3: Convergence study of first ordered mesh

mesh size	error	convergence rate
4/100	1.6e-3	
$2\sqrt{2}/100$	8.3e-4	1.89
2/100	4.0e-4	2.11
$\sqrt{2}/100$	1.7e-4	2.47

Table 4: Convergence study of second ordered mesh

mesh size	error	convergence rate
4/100	4.9e-4	
$2\sqrt{2}/100$	2.2e-4	2.31
2/100	8.1e-5	2.88
$\sqrt{2}/100$	2.3e-5	3.63

Obviously, the use of second-order mesh leads to a noticeable improvement in the convergence rate, the magnitude of the error is largely reduced as well. This proves that employing a second-order mesh in time-dependent FSI computations with smooth interface could provide significantly better accuracy. The above numerical examples provide strong evidence of the accuracy of our hybrid method in handling fluid–structure interaction problems involving large translational motions.

## 5.2 3D FSI simulation of a free falling sphere in fluid

Beyond demonstrating satisfactory performance in two-dimensional settings, the present model and its associated algorithm can be readily extended to three-dimensional cases.

Following the data provided in [37], we designed and performed a simulation of the free fall of a small sphere in a tank. The tank has dimensions of 100mm×100mm×160 mm. The sphere density is 1120 kg/m<sup>3</sup>, released from rest at point (50mm, 50mm, 120mm). Simulations were conducted for four liquids with different viscosity, and the respective parameters are listed in the table below. Non-slip boundary condition is applied to all the walls of the tank during simulation. The Young's modulus of the ball is set to be E=1e9 Pa to simulate a rigid body's motion

Table 5: Parameters of four different liquids

case	viscosity (Kg/m <sup>3</sup> )	density (Ns/m <sup>2</sup> )	Reynolds number
1	970	373	1.5
2	965	212	4.1
3	962	113	11.6
4	960	58	31.9

Figure 6 shows the simulation result of velocity field of case 1 at different time. The color represents the magnitude of the velocity field of both the ball and the fluid while the arrow near the ball shows the direction of the velocity field. Figure 7 (a) and (b) illustrate the time evolution of the sphere height-diameter ratio and the falling velocity, respectively, for the four simulated cases. Additionally, experimental data from [37] are included for comparison.

As can be seen from the sketch, the simulation result is highly consistent with the experimental data under different cases, indicating the proposed algorithm exhibits high numerical accuracy.

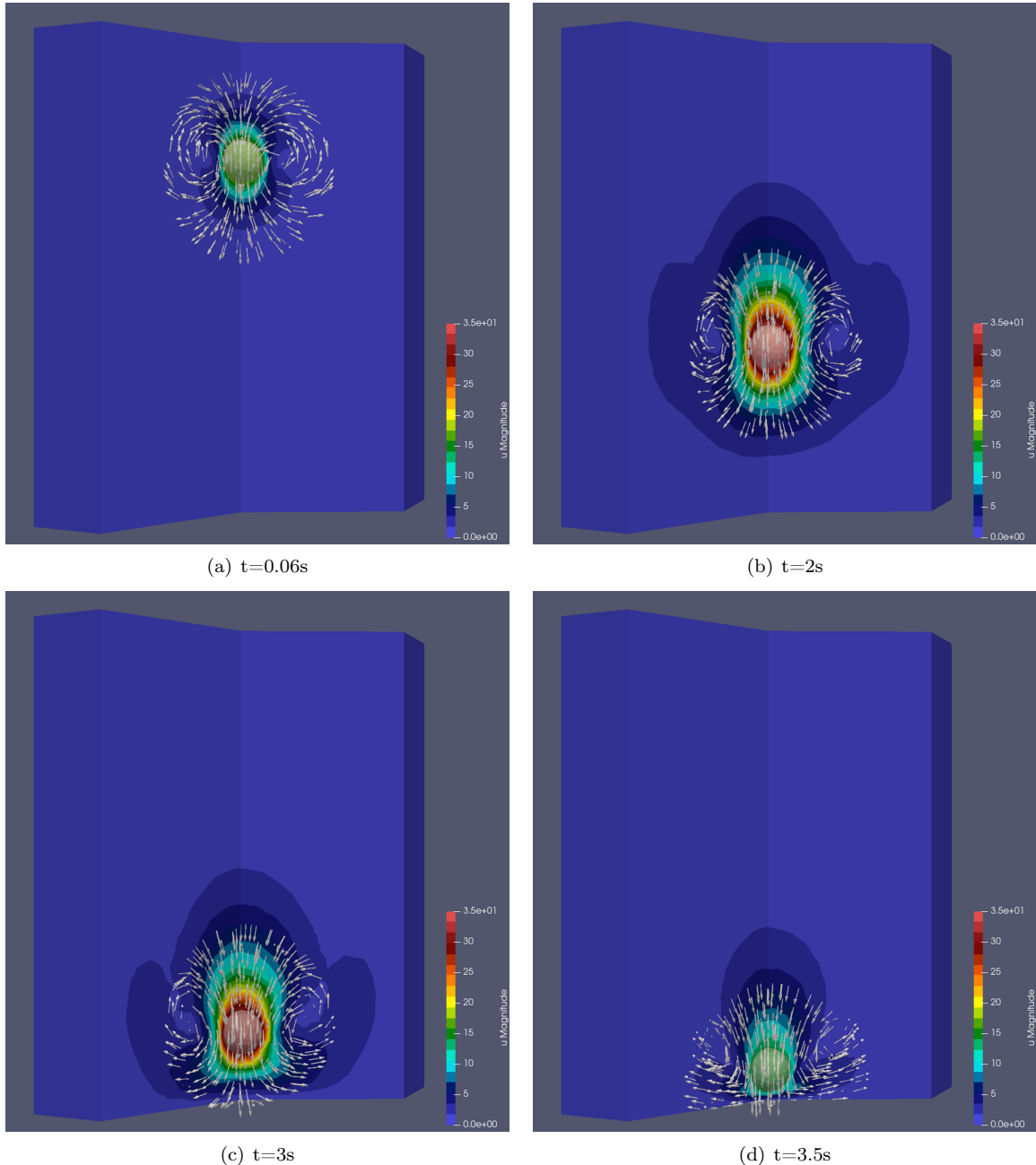


Figure 6: velocity field of the free falling ball in the fluid. the color shows the magnitude of the velocity field and the arrow located near the ball represents the direction of the velocity field.

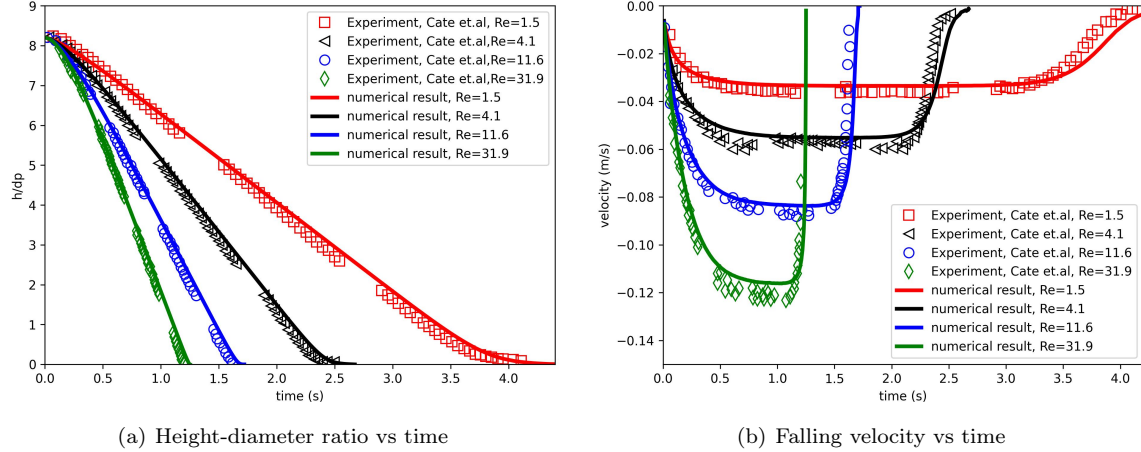


Figure 7: (a) Time evolution of vertical position presented as height-diameter ratio. (b) Time evolution of falling velocity. Experimental data from [37] is shown by symbols in the figure.

### 5.3 Multi-scale simulation in long spiral channel

Recently, as the number of reports on microfluidic devices is increasing fast, many studies have focused on the focusing and separation of particles in microchannels with spiral structures [4, 8, 19]. In some researches, obstacles are added inside the spiral channel in order to improve their performance [40, 33]. In this part, we will use the local updating algorithm to present the simulation results for these cases.

As shown in Figure 8 a spiral channel with obstacles are set. According to the reference above, the radius of the innermost circular arc is  $10000\mu\text{m}$ , which is typical scale in recent researches. The radius of the arc gradually increases, with each loop increasing by  $1350\mu\text{m}$ . The channel is  $900\mu\text{m}$  wide and  $100\mu\text{m}$  high. Each loop contains 14 obstacles with radius of  $450\mu\text{m}$ . The flow enters through the inner port and exits through the outer port. At the entrance velocity Dirichlet boundary condition is applied to ensure the flux of the channel is adjustable.

Figure 9 plotted the magnitude of velocity field at height  $50\mu\text{m}$  with flux  $1\text{mL/min}$ ,  $1.5\text{mL/min}$  and  $3\text{mL/min}$ . Particles with radius  $r = 4$  are released in the channel with 0 velocity initially at the inner loop, distributed uniformly along y-axis with  $z = -25\mu\text{m}$  and  $x = 0\mu\text{m}$ .

The FSI calculation is done by the local update algorithm in order to improve the efficiency of the simulation. The local domain extracted from the entire flow channel is shown in Figure 10 and presented together with the calculated velocity field.

Two loops are simulated and the trajectories of the particles are shown in Figure 11. It could be obviously observed that as the flux increases, the focusing of the particles is gradually enhanced.

## 6 Conclusion

In this work, we develop a high performance model and the corresponding algorithm for solving FSI simulation.

The hybrid method employs a sharp interface model, combined with second-order grids and isoparametric

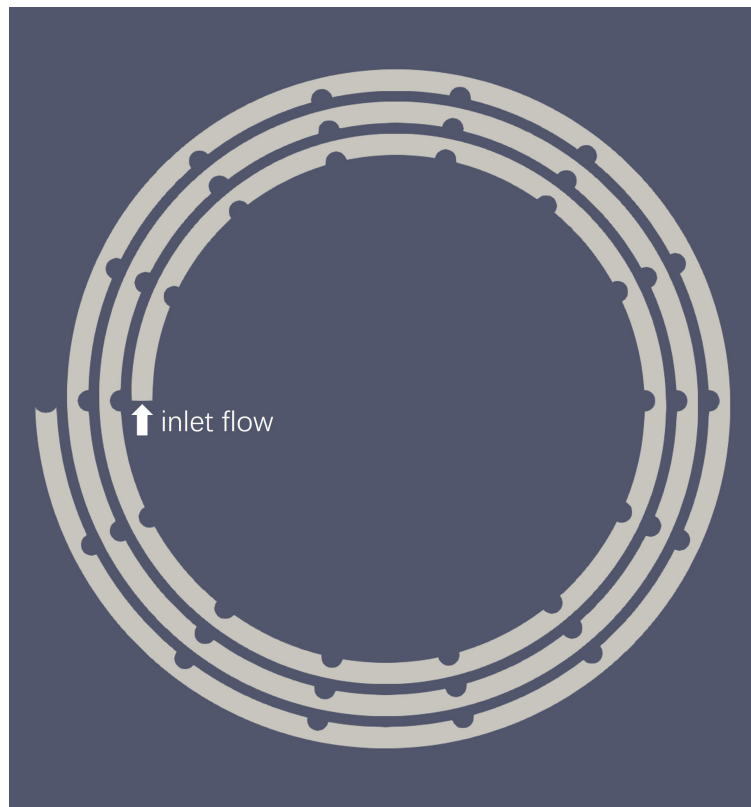


Figure 8: The background domain of the spiral channel.

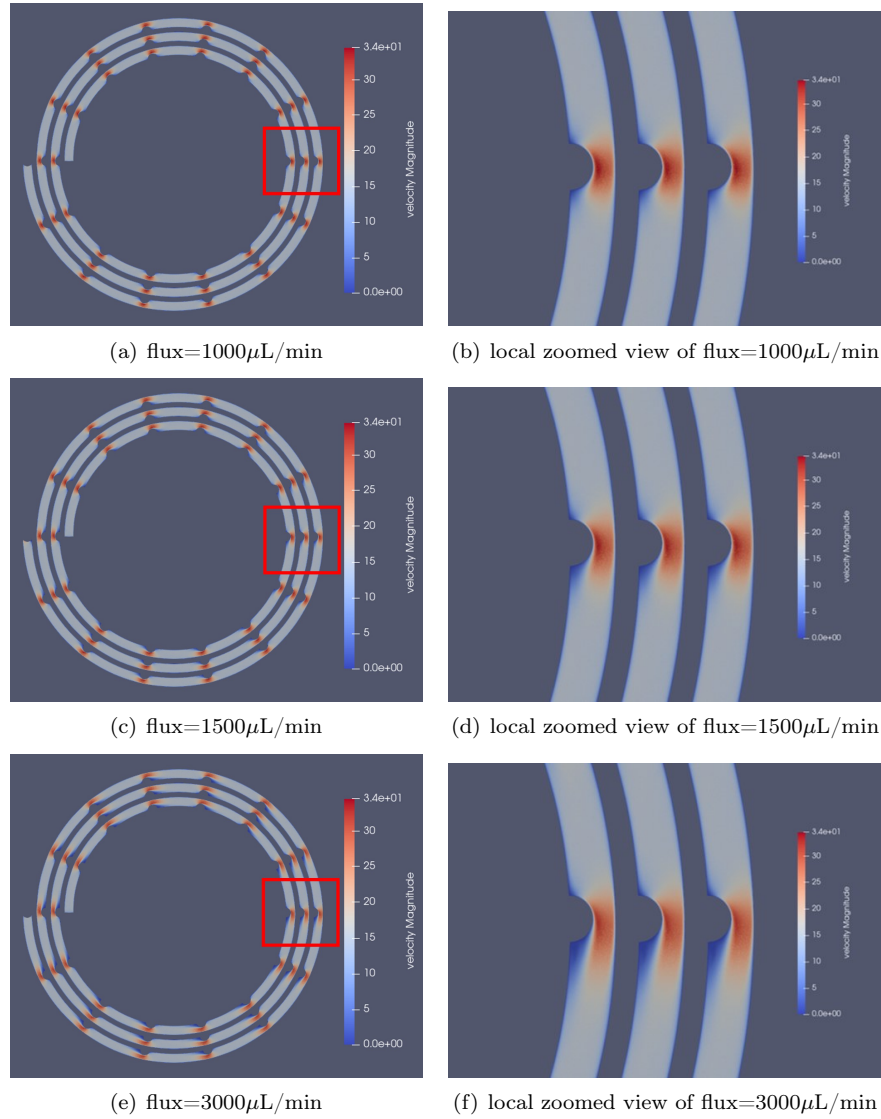
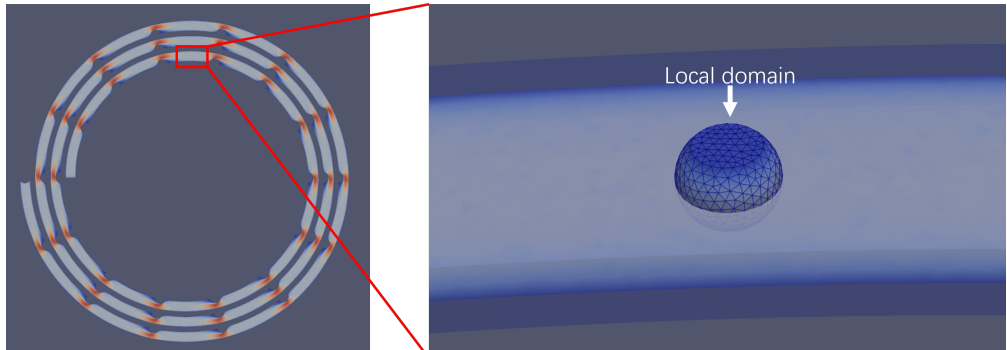
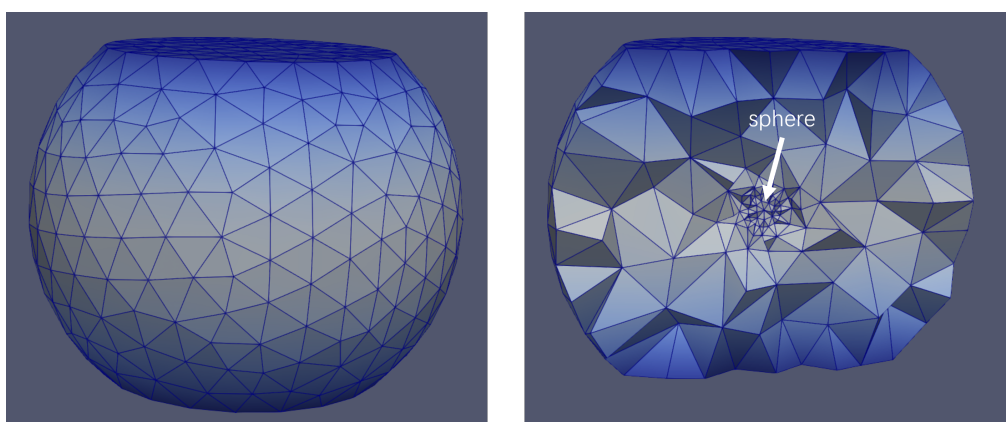


Figure 9: The magnitude of the velocity field on the cross-section of the flow channel with different flux (left) along with the zoomed views (right) of the local part in the red frame.

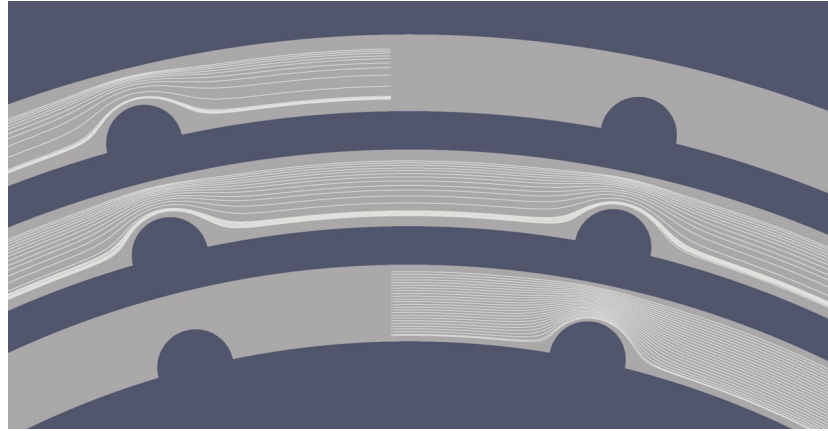


(a) Local domain extraction

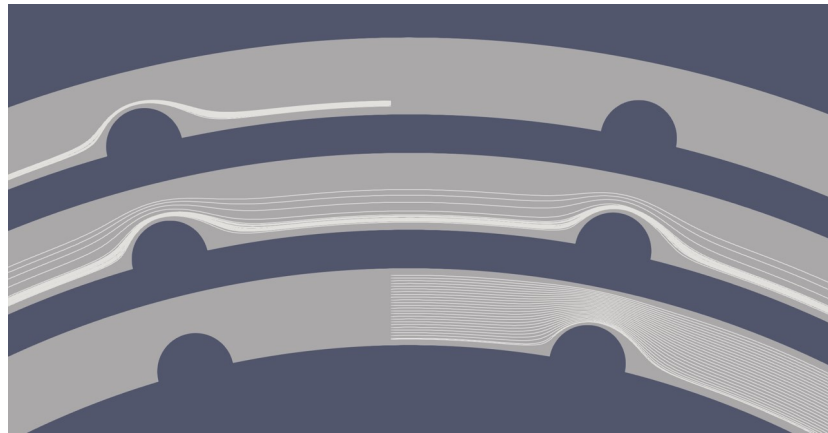


(b) Local domain and cross section together with velocity field

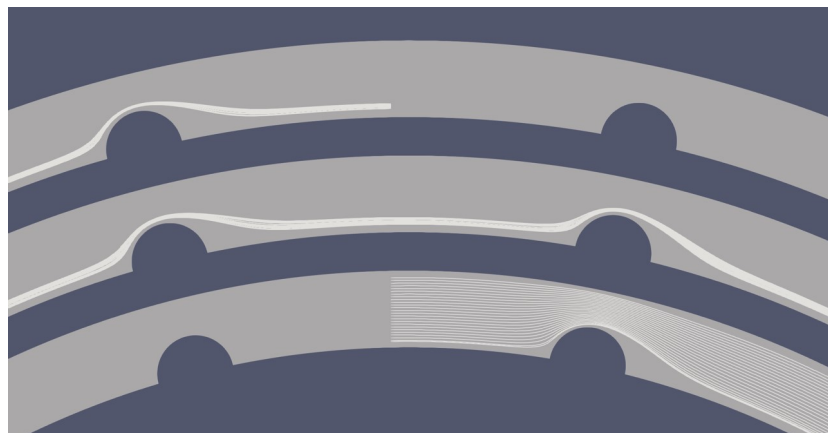
Figure 10: (a) Local domain extraction. As can be seen, there is a significant scale disparity between the flow channel and the local domain. (b) The mesh of local domain together with the cross section. The sphere is located in the center of the domain and the mesh size nearby is thinner. The calculated velocity field is also plotted on the meshes.



(a) The trajectories of particles released at with flux= $1000\mu\text{L}/\text{min}$



(b) The trajectories of particles released at with flux= $1500\mu\text{L}/\text{min}$



(c) The trajectories of particles released at with flux= $3000\mu\text{L}/\text{min}$

Figure 11: 25 particles are released at the inner loop of the channel at with  $z = -25\mu\text{m}$ . Two loops are traveled totally, as can be seen from the trajectories, the focusing phenomenon is increasingly clear as the flux in the channel increase.

finite elements, achieving exceptionally high convergence order in spatial discretization when simulating fluid–structure interactions with smooth interfaces, thereby ensuring superior accuracy. It offers significant advantages when applied to problems involving smooth or geometrically complex surfaces, which shows promising potential for application in aerospace and other engineering domains.

The incorporation of a moving mesh technique, along with the use of a second-order Runge–Kutta scheme, significantly enhances the algorithm’s ability to capture material trajectories under large translational motions over time. As a result, the trajectory accuracy reaches second-order precision in time. This makes it particularly suitable for applications requiring precise particle trajectory tracking, including various biomedical research scenarios such as the study of blood cell dynamics.

When simulating multi-scale FSI problems in steady background flows, the use of the local update algorithm could effectively reduce computational cost while maintaining satisfactory accuracy within the region of interest. It holds broad application prospects in research areas such as the development of microfluidic devices.

## References

- [1] TD AlMomani, SC Vigmostad, and LA Alzube. “A Sharp-Interface Fluid-Structure Interaction Algorithm for Modeling Red Blood Cells.” In: *Jordan Journal of Mechanical & Industrial Engineering* 6.2 (2012).
- [2] Uri M Ascher, Steven J Ruuth, and Raymond J Spiteri. “Implicit-explicit Runge-Kutta methods for time-dependent partial differential equations”. In: *Applied Numerical Mathematics* 25.2-3 (1997), pp. 151–167.
- [3] Sajjad Betyar and Abbas Ramiar. “Numerical Simulation of Biological Particle Separation in a Spiral Microchannel Using the Dielectrophoresis Mechanism”. In: *Iranica Journal of Energy & Environment* 17.1 (2026), pp. 171–179.
- [4] Jin Chen et al. “A microfluidic device integrating spiral focusing and micropillar filtration for Enhanced separation of Overlapping-Sized microparticles”. In: *Microchemical Journal* 208 (2025), p. 112570.
- [5] Arash Dalili, Ehsan Samiei, and Mina Hoorfar. “A review of sorting, separation and isolation of cells and microbeads for biomedical applications: microfluidic approaches”. In: *Analyst* 144.1 (2019), pp. 87–113.
- [6] Hamidreza Dehghani and Andreas Zilian. “Finite strain poro-hyperelasticity: an asymptotic multi-scale ALE-FSI approach supported by ANNs”. In: *Computational Mechanics* 71.4 (2023), pp. 695–719.
- [7] Kaan Erdem et al. “Differential sorting of microparticles using spiral microchannels with elliptic configurations”. In: *Micromachines* 11.4 (2020), p. 412.
- [8] Haidong Feng et al. “Viscoelastic particle focusing and separation in a spiral channel”. In: *Micromachines* 13.3 (2022), p. 361.
- [9] Karl Gardner et al. “Deep learning detector for high precision monitoring of cell encapsulation statistics in microfluidic droplets”. In: *Lab on a Chip* 22.21 (2022), pp. 4067–4080.
- [10] Bibek Gupta, Eric Sihite, and Alireza Ramezani. “Modeling and controls of fluid-structure interactions (FSI) in dynamic morphing flight”. In: *arXiv preprint arXiv:2406.13039* (2024).
- [11] Cyril W Hirt, Anthony A Amsden, and JL Cook. “An arbitrary Lagrangian-Eulerian computing method for all flow speeds”. In: *Journal of computational physics* 14.3 (1974), pp. 227–253.
- [12] Qi Hong and Qi Wang. “A hybrid phase field method for fluid-structure interactions in viscous fluids”. In: *arXiv preprint arXiv:2109.07361* (2021).
- [13] Mitsuhiro Horade et al. “Analysis of Separation Efficiency Focusing on Particle Concentration and Size Using a Spiral Microfluidic Device”. In: *Journal of Robotics and Mechatronics* 35.5 (2023), pp. 1203–1212.
- [14] Patrick Hu et al. “Material point method applied to fluid-structure interaction (FSI)/aeroelasticity problems”. In: *48th AIAA aerospace sciences meeting including the new horizons forum and aerospace exposition*. 2010, p. 1464.

[15] Shyam Sundar Jayakumar et al. “Design, control, aerodynamic performances, and structural integrity investigations of compact ducted drone with co-axial propeller for high altitude surveillance”. In: *Scientific Reports* 14.1 (2024), p. 6330.

[16] Shuyue Jiang et al. “On-chip label-free manipulation and enrichment of microparticles by utilizing DLD microfluidic chip”. In: *Journal of Physics: Conference Series*. Vol. 3021. 1. IOP Publishing. 2025, p. 012097.

[17] Vaibhav Joshi, Rajeev K Jaiman, and Carl Ollivier-Gooch. “A variational flexible multibody formulation for partitioned fluid–structure interaction: Application to bat-inspired drones and unmanned air-vehicles”. In: *Computers & Mathematics with Applications* 80.12 (2020), pp. 2707–2737.

[18] Christopher A Kennedy and Mark H Carpenter. “Additive Runge–Kutta schemes for convection–diffusion–reaction equations”. In: *Applied numerical mathematics* 44.1-2 (2003), pp. 139–181.

[19] Tharagan Kumar et al. “High throughput viscoelastic particle focusing and separation in spiral microchannels”. In: *Scientific reports* 11.1 (2021), p. 8467.

[20] Sang-Gab Lee et al. “Full-scale ship collision, grounding and sinking simulation using highly advanced M&S system of FSI analysis technique”. In: *Procedia engineering* 173 (2017), pp. 1507–1514.

[21] Xiong Li et al. “Numerical Simulation and Analysis of Heart–Aorta Fluid–Structure Interaction Based on S-ALE Method”. In: *Applied Sciences* 15.14 (2025), p. 7769.

[22] Chun Liu and Noel J Walkington. “An Eulerian description of fluids containing visco-elastic particles”. In: *Archive for rational mechanics and analysis* 159.3 (2001), pp. 229–252.

[23] Zongbin Liu et al. “Cascaded filter deterministic lateral displacement microchips for isolation and molecular analysis of circulating tumor cells and fusion cells”. In: *Lab on a Chip* 21.15 (2021), pp. 2881–2891.

[24] Xiaoyu Mao, Biswajeet Rath, and Rajeev Jaiman. “A 3D phase-field based Eulerian variational framework for multiphase fluid–structure interaction with contact dynamics”. In: *Computer Methods in Applied Mechanics and Engineering* 429 (2024), p. 117172.

[25] Wieland Marth, Sebastian Aland, and Axel Voigt. “Margination of white blood cells: a computational approach by a hydrodynamic phase field model”. In: *Journal of fluid mechanics* 790 (2016), pp. 389–406.

[26] Rajat Mittal and Gianluca Iaccarino. “Immersed boundary methods”. In: *Annu. Rev. Fluid Mech.* 37.1 (2005), pp. 239–261.

[27] Rohollah Nasiri et al. “Microfluidic-based approaches in targeted cell/particle separation based on physical properties: fundamentals and applications”. In: *Small* 16.29 (2020), p. 2000171.

[28] Arzu Özbeý et al. “Inertial focusing of microparticles in curvilinear microchannels”. In: *Scientific Reports* 6.1 (2016), p. 38809.

[29] Charles S Peskin. “Numerical analysis of blood flow in the heart”. In: *Journal of computational physics* 25.3 (1977), pp. 220–252.

[30] Omkar Powar et al. “Recent Developments in the Immersed Boundary Method for Complex Fluid–Structure Interactions: A Review”. In: *Fluids* 10.5 (2025), p. 134.

- [31] Biswajeet Rath and Rajeev K Jaiman. “A Phase Field Formulation of Frictional Sliding Contact for 3D Fully Eulerian Fluid Structure Interactions”. In: *arXiv preprint arXiv:2509.11611* (2025).
- [32] Biswajeet Rath, Xiaoyu Mao, and Rajeev K Jaiman. “An Interface-Driven Adaptive Variational Procedure for Fully Eulerian Fluid-Structure Interaction via Phase-field Modeling”. In: *arXiv preprint arXiv:2112.15309* (2021).
- [33] Shaofei Shen et al. “Spiral large-dimension microfluidic channel for flow-rate-and particle-size-insensitive focusing by the stabilization and acceleration of secondary flow”. In: *Analytical Chemistry* 96.4 (2024), pp. 1750–1758.
- [34] Ming Song, Jun Ma, and Yi Huang. “Fluid-structure interaction analysis of ship-ship collisions”. In: *Marine Structures* 55 (2017), pp. 121–136.
- [35] Fotis Sotiropoulos and Xiaolei Yang. “Immersed boundary methods for simulating fluid–structure interaction”. In: *Progress in Aerospace Sciences* 65 (2014), pp. 1–21.
- [36] Faiz Syed, Sahar Khan, and Milan Toma. “Modeling dynamics of the cardiovascular system using fluid-structure interaction methods”. In: *Biology* 12.7 (2023), p. 1026.
- [37] A Ten Cate et al. “Particle imaging velocimetry experiments and lattice-Boltzmann simulations on a single sphere settling under gravity”. In: *Physics of Fluids* 14.11 (2002), pp. 4012–4025.
- [38] Fang-Bao Tian et al. “An FSI solution technique based on the DSD/SST method and its applications”. In: *Mathematical Models and Methods in Applied Sciences* 25.12 (2015), pp. 2257–2285.
- [39] LL Xiao et al. “Effects of flowing RBCs on adhesion of a circulating tumor cell in microvessels”. In: *Biomechanics and modeling in mechanobiology* 16.2 (2017), pp. 597–610.
- [40] Lei Zhao et al. “Flow-rate and particle-size insensitive inertial focusing in dimension-confined ultra-low aspect ratio spiral microchannel”. In: *Sensors and Actuators B: Chemical* 369 (2022), p. 132284.
- [41] Zhenyu Zhao et al. “Injectable microfluidic hydrogel microspheres for cell and drug delivery”. In: *Advanced Functional Materials* 31.31 (2021), p. 2103339.